

The coupled dipole model: an integrated model for multiple MEG/EEG data sets

Fetsje Bijma,^{a,*} Jan C. de Munck,^a Koen B.E. Böcker,^b
Hilde M. Huizenga,^c and Rob M. Heethaar^d

^aMEG Center, Department Physics and Medical Technology, VU University Medical Center, 1081 HZ Amsterdam, The Netherlands

^bDepartment of Psychopharmacology, Utrecht University, PO Box 80082, 3508 TB Utrecht, The Netherlands

^cDepartment of Developmental Psychology, University of Amsterdam, 1018 WB Amsterdam, The Netherlands

^dDepartment Physics and Medical Technology, VU University Medical Center, 1081 HZ Amsterdam, The Netherlands

Received 18 December 2003; revised 3 March 2004; accepted 22 June 2004

Available online 2 October 2004

Often MEG/EEG is measured in a few slightly different conditions to investigate the functionality of the human brain. This kind of data sets show similarities, though are different for each condition. When solving the inverse problem (IP), performing the source localization, one encounters the problem that this IP is ill-posed: constraints are necessary to solve and stabilize the solution to the IP. Moreover, a substantial amount of data is needed to avoid a signal to noise ratio (SNR) that is too poor for source localizations.

In the case of similar conditions, this common information can be exploited by analyzing the data sets simultaneously. The here proposed coupled dipole model (CDM) provides an integrated method in which these similarities between conditions are used to solve and stabilize the inverse problem. The coupled dipole model is applicable when data sets contain common sources or common source time functions.

The coupled dipole model uses a set of common sources and a set of common source time functions (STFs) to model all conditions in one single model. The data of each condition are mathematically described as a linear combination of these common spatial and common temporal components. This linear combination is specified in a coupling matrix for each data set.

The coupled dipole model was applied in two simulation studies and in one experimental study. The simulations show that the errors in the estimated spatial and temporal parameters decrease compared to the standard separate analyses. A decrease in position error of a factor of 10 was shown for the localization of two nearby sources. In the experimental application, the coupled dipole model was shown to be necessary to obtain a plausible solution in at least 3 of 15 conditions investigated. Moreover, using the CDM, a direct comparison between parameters in different conditions is possible, whereas in separate

models, the scaling of the amplitude parameters varies in general from data set to data set.

© 2004 Elsevier Inc. All rights reserved.

Keywords: MEG/EEG source analysis; Integrated model; Trilinear model; Spatiotemporal covariance; Coupled dipole model; Visual evoked field; Component model

Introduction

To investigate the functionality of the human brain, MEG/EEG is often measured in a few different but similar conditions. This way, the influence of a certain experimental parameter on the activity of the brain can be examined. For example, a common experimental paradigm for investigation of the visual cortex is the presentation of checkerboard patterns in different visual fields using varying check sizes. In this kind of experiments, the measured MEG/EEG data of the different conditions will be different, though there are similarities too.

In the source localization of these data, the inverse problem (IP) of MEG/EEG, these similarities can be exploited. The IP is in general ill-posed; assumptions (e.g., head model, source model, number of sources) are necessary to solve the problem. Moreover, often extra constraints (e.g., mirror symmetry) are needed to stabilize the IP. Secondly, a low signal to noise ratio (SNR) results in unstable solutions to the IP. The SNR of single trials in MEG/EEG measurements is usually too poor to perform source localization on single trial basis. Therefore, a first approach to take more data into account is to average repeated measurements to increase the SNR. Finally, a third problem with solving the IP using the common equivalent current dipole source model is instability due to nearby sources: two closely localized dipole sources having nearly opposite orientations and unrealistically high magnitudes.

* Corresponding author. MEG Center, Department PMT, VU University Medical Center, De Boelelaan 1118, 1081 HZ Amsterdam, The Netherlands. Fax: +31 20 4444147.

E-mail address: f.bijma@vumc.nl (F. Bijma).

Available online on ScienceDirect (www.sciencedirect.com.)

In the case of similar conditions, the IP can be stabilized using a component model. A component model uses a set of basic spatial and temporal components and the data are described as linear combinations of (some of) these basic components. The similarity between conditions is reflected in the usage of the same basic components in different conditions.

Component models have been designed before. The topographic component model (TCM) (Möcks, 1988) decomposes EEG data of multiple subjects into a sum of topographic components, each component consisting of a scalp distribution and a (nonparametric) time series. In Field and Graupe (1991), the TCM is applied to real data. Extensions of the TCM can be found in Achim and Bouchard (1997), Turetsky et al. (1990), and Wang et al. (2000).

Turetsky et al. (1990) extend the TCM by using dipolar sources (Scherg and Von Cramon, 1985) as spatial components and parametric, predefined time courses to describe data of different subjects. In Achim and Bouchard (1997), the TCM is extended by allowing different durations and different latencies of the temporal components for each condition. Wang et al. (2000) decouple the spatial and temporal components and introduce a trilinear model with so-called loading matrices. In this trilinear model, the number of spatial components can be different from the number of temporal components, and these loading matrices are placed in between the spatial and the temporal matrices. The spatial components in Wang et al. (2000) are again described by scalp distributions instead of the more elementary dipole sources.

Although in some of these studies the correlations of the background activity are mentioned (Achim and Bouchard, 1997; Turetsky et al., 1990), these correlations are neglected in the estimation of the components and the remaining parameters. Therefore, these estimation methods seem somewhat ad hoc; a clearly defined statistical framework is not given.

We designed a new component model, the coupled dipole model (CDM), that resembles in a way the trilinear model in Wang et al. (2000), but is still fundamentally different. The main difference is in the basic idea of the model: the CDM is a parameter estimation method based on the well-defined maximum likelihood (ML) framework. Moreover, the correlations of the background activity are in this way taken into account in the source localization, which was recently shown to improve the source parameters compared to the ordinary least squares approach (De Munck et al., 2002; Huizenga et al., 2002).

The basic spatial components of the CDM are dipole sources, and the basic temporal components are nonparametric time series. The data of each condition is modeled as a linear combination of

the basic components. This linear combination is specified by a coupling matrix for each condition, comparable to Wang’s loading matrix. However, contrary to the model in Wang et al. (2000), all parameters (spatial, temporal, and coupling parameters) are estimated simultaneously using the maximum likelihood paradigm, instead of successively using different singular value decompositions of the rearranged data.

The CDM is applicable when the different conditions contain common information: either common sources or common source time series. In this integrated approach, a combination of more data and more constraints is used to solve and stabilize the IP: sources and/or source time series are assumed to be fixed over (part of the) conditions.

In the next section, the coupled dipole model is explained. Then the results of the application of the CDM in two MEG simulation studies and in an experimental visual evoked response MEG-study are shown.

Methods

Model

In the coupled dipole model, each data set is modeled as a linear combination of basic sources (equivalent current dipoles) and basic source time functions (STFs). This linear combination is specified in the coupling matrix C_q for each data set q . The coupling matrices contain the amplitudes of the components, which may vary over data sets.

If there are I sensors and J time samples, then the measured signal of trial k in data set q is stored in the $I \times J$ matrix R_q^k , for $q = 1, \dots, Q$, $k = 1, \dots, K_q$. Furthermore, if the number of basic spatial components is P and the number of basic temporal components is Z , the basic field matrix A is the $I \times P$ matrix containing the forward fields of the basic dipole sources (DF), and the basic source time function matrix B is the $Z \times J$ matrix containing all basic STFs as rows. The model for data set q is then

$$R_q = AC_qB, \tag{1}$$

where $A = A(\xi, \eta)$ is dependent on the source locations ξ and the source orientations η . The coupling matrices C_q have dimension $P \times Z$. The reader is referred to Appendix A for a full list of dimensions and variables. In Fig. 1, the CDM formula is illustrated.

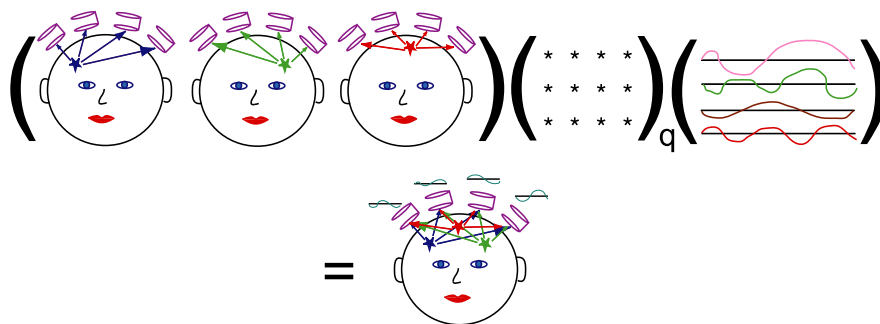


Fig. 1. Illustration of the Coupled Dipole Model. The first matrix contains the fields of the basic sources (i.e. the contribution of the basic sources to each of the sensors), the second matrix is the coupling matrix and the last matrix is the basic time series matrix. The model for each data set, the product of these matrices, is a linear combination of the depicted basic components, as indicated in the lower picture.

The CDM provides a general framework that can describe different situations in a flexible way by specifying which entries of C_q are zero and which entries have to be estimated from the data. A simple illustration would consist of two data sets ($Q = 2$), in which one source is active ($P = 1$). The source time function is different in both data sets ($Z = 2$). The matrices A and B of the CDM in this example would then have dimensions $I \times 1$ and $2 \times J$, respectively. Moreover, the coupling matrices C_1 and C_2 are 1×2 matrices.

$$A = (DF_1), B = \begin{pmatrix} STF_1 \\ STF_2 \end{pmatrix}, C_1 = (\alpha_1 \ 0), C_2 = (0 \ \alpha_2) \quad (2)$$

The models for both data sets are

$$R_1 = AC_1B = (DF_1) \times (\alpha_1 STF_1)$$

and

$$R_2 = AC_2B = (DF_1) \times (\alpha_2 STF_2).$$

In the CDM, the basic source parameters, the amplitudes in the coupling matrices, and the nonparametric basic source time functions are estimated. For each data set, the linear combination of basic components, characterized by the coupling matrix, has to be specified by the researcher.

Moreover, the dimension of the coupling matrices (i.e., the number of basic components) has to be set. In other words, the dimensions and the zero elements of the coupling matrices are set by the researcher, while the nonzero elements (amplitude parameters) are estimated from the data. Fewer (more) assumptions regarding the common components in the data are reflected by bigger (smaller) dimensions of the coupling matrices and/or fewer (more) zeroes in the coupling matrices defined. In the extreme case of no assumptions on common components, the dimension of the coupling matrices would be maximum (for each data set separately, spatial and temporal components would be estimated) and each coupling matrix would contain only a few, diagonal nonzero entries, coupling the corresponding spatial and temporal components. In the example (2) above, making no assumptions would lead to estimation of two sources ($P = 2$) and two STFs ($Z = 2$) and using two 2×2 coupling matrices:

$$A = (DF_1 \ DF_2), B = \begin{pmatrix} STF_1 \\ STF_2 \end{pmatrix}, C_1 = \begin{pmatrix} \alpha_1 & 0 \\ 0 & 0 \end{pmatrix}, \\ C_2 = \begin{pmatrix} 0 & 0 \\ 0 & \alpha_2 \end{pmatrix} \quad (3)$$

And the models for both data sets would become

$$R_1 = AC_1B = (DF_1) \times (\alpha_1 STF_1)$$

and

$$R_2 = AC_2B = (DF_2) \times (\alpha_2 STF_2).$$

The nonzero elements in all coupling matrices are the amplitudes, which are estimated from the data. For all data sets

q , $C_q = C_q(\underline{\alpha})$ is dependent on $\underline{\alpha}$, the $Y \times 1$ vector containing all amplitudes (coupling parameters). These coupling parameters determine the magnitude of the temporal components, while the basic STFs in B are normalized, that is, each row in B has norm 1.

Probability density function

When brain activity is evoked by a stimulus, measured data consists, according to the signal plus noise model, of a constant brain response and additional (internal and external) noise (Bijma et al., 2003; De Munck et al., in press; McGillem and Aunon, 1987). If R_q^k denotes the measured data matrix in trial k of data set q , this can be formulated as

$$R_q^k = R_q + E_q^k \quad (4)$$

where we write R_q for the constant response matrix in data set q and E_q^k for the measured noise matrix. Furthermore, $\text{vec}(E_q^k)^t$ is assumed to have a Gaussian distribution, to be independent over trials $k = 1, \dots, K_q$ and to have the Kronecker product of a spatial covariance matrix X and a temporal covariance matrix T as spatiotemporal covariance (De Munck et al., 1992, 2002; Huizenga et al., 2002), where X and T are constant over k :

$$\text{vec}\left(\left(E_q^k\right)^t\right) \sim \mathcal{N}(0, X \otimes T) \text{ for all } k. \quad (5)$$

Thus, we obtain the likelihood function for data set q (see Magnus and Neudecker, 1995, for handling formulas with Kronecker Products)

$$L_q(X, T, \underline{\xi}, \underline{\eta}, \underline{\alpha}, B) = \frac{1}{(2\pi)^{\frac{IK_q}{2}}} \frac{1}{|X|^{\frac{JK_q}{2}}} \\ \times \frac{1}{|T|^{\frac{IK_q}{2}}} e^{-\frac{1}{2} \text{tr} \left[\sum_{k=1}^{K_q} (R_q^k - AC_qB)^t X^{-1} (R_q^k - AC_qB) T^{-1} \right]}. \quad (6)$$

When the noise covariances X and T are known, this likelihood function is only a function of $\underline{\xi}$, $\underline{\eta}$, $\underline{\alpha}$, and B . In practice, different data sets are measured in different trials, and thus independency of E_q^k over trials leads to independency over data sets too. Furthermore, X and T are assumed to be fixed over data sets. This yields the total likelihood function for all data sets, $L(X, T, \underline{\xi}, \underline{\eta}, \underline{\alpha}, B)$, which is the product of the likelihood functions L_q in (6):

$$L(X, T, \underline{\xi}, \underline{\eta}, \underline{\alpha}, B) = \prod_{q=1}^Q L_q(X, T, \underline{\xi}, \underline{\eta}, \underline{\alpha}, B) = \frac{1}{(2\pi)^{\frac{IK}{2}}} \frac{1}{|X|^{\frac{JK}{2}}} \\ \times \frac{1}{|T|^{\frac{IK}{2}}} e^{-\frac{1}{2} \text{tr} \left[\sum_{q=1}^Q \sum_{k=1}^{K_q} (R_q^k - AC_qB)^t X^{-1} (R_q^k - AC_qB) T^{-1} \right]}. \quad (7)$$

By maximizing Eq. (7) the maximum likelihood (ML) estimators for the noise parameters, X and T and the signal parameters $\underline{\xi}$, $\underline{\eta}$, $\underline{\alpha}$, and B are derived.

ML-estimation procedure

The ML estimators \hat{X} , \hat{T} , $\hat{\eta}$, $\hat{\xi}$, $\hat{\alpha}$, and \hat{B} are derived from Eq. (7) by setting the corresponding derivative equal to zero and solving for the estimated parameters. Differentiation of Eq. (7) is performed using the rules derived in Magnus and Neudecker (1995), chapter 9. This yields a complicated system of equations for the estimators: all estimators are expressed in terms of each other and have to be solved iteratively. The estimator for $\hat{\xi}$ is even more complex because $\hat{\xi}$ is a nonlinear parameter. To simplify this estimation procedure, the iterative system is split into two parts as in De Munck et al. (2002). In the first preparative step, the noise parameters are estimated, and in the second, the signal parameters. In the case of known X and T (e.g., based on previous data sets), the first step is left out.

In the first step, the expression AC_qB has to be replaced because the model parameters are not yet determined in that step. The substituting term is the ML estimator for AC_qB as a whole:

$$\left(\widehat{AC_qB}\right)_{ML} = \frac{1}{K_q} \sum R_q^k =: \bar{R}_q \quad (8)$$

Substituting Eq. (8) in Eq. (7) and taking the derivative with respect to the noise parameters, X and T , yields (see Appendix B):

$$\hat{X}_{ML} = \frac{1}{JK} \sum_{q=1}^Q \sum_{k=1}^{K_q} \left(R_q^k - \bar{R}_q\right) \hat{T}_{ML}^{-1} \left(R_q^k - \bar{R}_q\right)^t \quad (9)$$

$$\hat{T}_{ML} = \frac{1}{IK} \sum_{q=1}^Q \sum_{k=1}^{K_q} \left(R_q^k - \bar{R}_q\right)^t \hat{X}_{ML}^{-1} \left(R_q^k - \bar{R}_q\right) \quad (10)$$

The system consisting of Eqs. (9) and (10) is solved iteratively, starting with $T = \mathbf{I}_J$ in Eq. (9) until convergence of X and T . \mathbf{I}_J denotes the identity matrix of dimension J .

In the second step of the parameter estimation, either the true X and T or the estimators \hat{X}_{ML} and \hat{T}_{ML} , which are assumed to be the true covariances, are substituted in the likelihood function (7). For notational simplicity, the subscript ML will be omitted in the sequel. The likelihood has to be maximized with respect to ξ , η , B , and α , which is equivalent to the minimization of the cost function $H(\xi, \eta, B, \alpha)$:

$$\begin{aligned} H(\xi, \eta, B, \alpha) &= tr \left[\sum_{q=1}^Q \sum_{k=1}^{K_q} \left(R_q^k - AC_qB\right)^t \hat{X}^{-1} \left(R_q^k - AC_qB\right) \hat{T}^{-1} \right] \\ &= tr \left[\sum_{q=1}^Q K_q \left(\bar{R}_q - AC_qB\right)^t \hat{X}^{-1} \left(\bar{R}_q - AC_qB\right) \hat{T}^{-1} \right] + \gamma, \end{aligned} \quad (11)$$

where

$$\gamma = \sum_{q=1}^Q \left(\sum_{k=1}^{K_q} tr \left[\left(R_q^k\right)^t \hat{X}^{-1} R_q^k \hat{T}^{-1} \right] - K_q tr \left[\bar{R}_q^t \hat{X}^{-1} \bar{R}_q \hat{T}^{-1} \right] \right). \quad (12)$$

Clearly, γ does not depend on the signal parameters, and the cost function $H(\xi, \eta, B, \alpha)$ can be replaced by $\tilde{H}(\xi, \eta, B, \alpha)$:

$$\begin{aligned} \tilde{H}(\xi, \eta, B, \alpha) &= tr \left[\sum_{q=1}^Q K_q \left(\bar{R}_q - AC_qB\right)^t \hat{X}^{-1} \left(\bar{R}_q - AC_qB\right) \hat{T}^{-1} \right]. \end{aligned} \quad (13)$$

Setting the derivatives of \tilde{H} with respect to η , B , and α to zero yields the following ML estimators (the reader is referred to Appendices C to E for the mathematical derivations):

$$\hat{B}_{ML} = \left(\sum_{q=1}^Q K_q C_q^t A^t \hat{X}^{-1} A C_q \right)^{-1} \sum_{q=1}^Q \sum_{k=1}^{K_q} C_q^t A^t \hat{X}^{-1} \left(R_q^k\right)^t \quad (14)$$

$$\Phi \hat{\eta}_{ML} = \phi \quad (15)$$

$$\Psi \hat{\alpha}_{ML} = \psi \quad (16)$$

where

$$\Phi_{p_1, p_2} = tr \left[\sum_{q=1}^Q K_q C_q B \hat{T}^{-1} B^t C_q^t \frac{\partial A^t}{\partial \eta_{p_2}} \hat{X}^{-1} \frac{\partial A}{\partial \eta_{p_1}} \right] \quad (17)$$

$$\phi_p = tr \left[\sum_{q=1}^Q \sum_{k=1}^{K_q} C_q B \hat{T}^{-1} \left(R_q^k\right)^t \hat{X}^{-1} \frac{\partial A}{\partial \eta_p} \right] \quad (18)$$

$$\Psi_{y_1, y_2} = tr \left[\sum_{q=1}^Q K_q B \hat{T}^{-1} B^t \frac{\partial C_q^t}{\partial \alpha_{y_2}} A^t \hat{X}^{-1} A \frac{\partial C_q}{\partial \alpha_{y_1}} \right] \quad (19)$$

$$\psi_y = tr \left[\sum_{q=1}^Q \sum_{k=1}^{K_q} B \hat{T}^{-1} \left(R_q^k\right)^t \hat{X}^{-1} A \frac{\partial C_q}{\partial \alpha_y} \right]. \quad (20)$$

The source positions $\hat{\xi}$ are determined in a nonlinear search algorithm.

The dimensionality of the problem can be reduced by using the singular value decomposition (SVD) of the data (cf. De Munck et al., 2002). To take advantage of the vanishing, small eigenvalues of the data, the data are rearranged.

For that purpose, the following decompositions of the covariance matrices are used

$$\hat{X}^{-1} = W_X W_X^t, \quad \hat{T}^{-1} = W_T W_T^t. \quad (21)$$

Furthermore, we define

$$\mathbf{R} := \begin{pmatrix} \sqrt{K_1} W_X^t \bar{R}_1 W_T \\ \vdots \\ \sqrt{K_Q} W_X^t \bar{R}_Q W_T \end{pmatrix}, \quad \mathbf{C} := \begin{pmatrix} \sqrt{K_1} C_1 \\ \vdots \\ \sqrt{K_Q} C_Q \end{pmatrix}, \quad (22)$$

$$\mathbf{A} := W_X^t A, \quad \mathbf{B} := B W_T.$$

Then Eq. (13) can be rewritten as

$$\begin{aligned} \tilde{H}(\underline{\xi}, \underline{\eta}, B, \underline{\alpha}) \\ = \text{tr} \left[(\mathbf{R} - (\mathbf{I}_Q \otimes \mathbf{A})\mathbf{C}\mathbf{B})^t (\mathbf{R} - (\mathbf{I}_Q \otimes \mathbf{A})\mathbf{C}\mathbf{B}) \right]. \end{aligned} \quad (23)$$

Now the SVD of \mathbf{R} , containing the stacked prewhitened data of all data sets, is calculated

$$\mathbf{R} = U\Delta V^t \text{ with } \begin{cases} U \in \mathbb{R}^{IQ \times J} & U^t U = \mathbf{I}_J \\ V \in \mathbb{R}^{J \times J} & V V^t = V^t V = \mathbf{I}_J \\ \Delta \in \mathbb{R}^{J \times J} & \Delta = \text{diag}(\lambda_1, \lambda_2, \dots, \lambda_J) \end{cases} \quad (24)$$

and Eq. (23) is rewritten

$$\begin{aligned} \tilde{H}(\underline{\xi}, \underline{\eta}, B, \underline{\alpha}) \\ = \text{tr} \left[(U\Delta - (\mathbf{I}_Q \otimes \mathbf{A})\mathbf{C}\mathbf{B}V)^t (U\Delta - (\mathbf{I}_Q \otimes \mathbf{A})\mathbf{C}\mathbf{B}V) \right]. \end{aligned} \quad (25)$$

The trace in Eq. (25) is split into terms corresponding to the first J_0 largest eigenvalues of \mathbf{R} and the remaining $J - J_0$ terms:

$$\begin{aligned} \tilde{H}(\underline{\xi}, \underline{\eta}, B, \underline{\alpha}) = \sum_{l=1}^{IQ} \sum_{j=1}^{J_0} (U\Delta - (\mathbf{I}_Q \otimes \mathbf{A})\mathbf{C}\mathbf{B}V)_{lj}^2 \\ + \sum_{l=1}^{IQ} \sum_{j=J_0+1}^J (U\Delta - (\mathbf{I}_Q \otimes \mathbf{A})\mathbf{C}\mathbf{B}V)_{lj}^2 \end{aligned} \quad (26)$$

The dimensionality of the estimation problem is reduced by setting the $J - J_0$ small eigenvalues of \mathbf{R} to zero and choosing \mathbf{B} such that $[(\mathbf{I}_Q \otimes \mathbf{A})\mathbf{C}\mathbf{B}V]_{lj} = 0$ for $j > J_0$ for all l . Then the second term in Eq. (26) will vanish and the remaining cost function is

$$\tilde{H}(\underline{\xi}, \underline{\eta}, B, \underline{\alpha}) = \sum_{l=1}^{IQ} \sum_{j=1}^{J_0} \left(U\Delta - (\mathbf{I}_Q \otimes \mathbf{A})\mathbf{C}\mathbf{B}V \right)_{lj}^2. \quad (27)$$

If the $J \times J$ truncated diagonal matrix is denoted by

$$\Delta_0 = \text{diag}(\lambda_1, \lambda_2, \dots, \lambda_{J_0}, 0, \dots, 0) \quad (28)$$

the estimators in Eqs. (14) and (17) to (20) change accordingly into

$$\hat{\mathbf{B}}_{ML} = \left(\mathbf{C}^t (\mathbf{I}_Q \otimes \mathbf{A}^t \mathbf{A}) \mathbf{C} \right)^{-1} \mathbf{C}^t (\mathbf{I}_Q \otimes \mathbf{A}^t) U \Delta_0 V^t \quad (29)$$

$$\Phi_{p_1, p_2} = \text{tr} \left[\mathbf{B}^t \mathbf{C}^t \left(\mathbf{I}_Q \otimes \frac{\partial \mathbf{A}^t}{\partial \eta_{p_2}} \right) \left(\mathbf{I}_Q \otimes \frac{\partial \mathbf{A}^t}{\partial \eta_{p_1}} \right) \mathbf{C}\mathbf{B} \right] \quad (30)$$

$$\phi_p = \text{tr} \left[V^t \mathbf{B}^t \mathbf{C}^t \left(\mathbf{I}_Q \otimes \frac{\partial \mathbf{A}^t}{\partial \eta_p} \right) U \Delta_0 \right] \quad (31)$$

$$\Psi_{y_1, y_2} = \text{tr} \left[\mathbf{B}^t \frac{\partial \mathbf{C}^t}{\partial \alpha_{y_2}} (\mathbf{I}_Q \otimes \mathbf{A}^t) (\mathbf{I}_Q \otimes \mathbf{A}) \frac{\partial \mathbf{C}}{\partial \alpha_{y_1}} \mathbf{B} \right] \quad (32)$$

$$\psi_y = \text{tr} \left[V^t \mathbf{B}^t \frac{\partial \mathbf{C}^t}{\partial \alpha_y} (\mathbf{I}_Q \otimes \mathbf{A}^t) U \Delta_0 \right]. \quad (33)$$

Summarizing, the estimation procedure looks like

- (1) Compute \bar{R}_q for all q and \hat{X} and \hat{T} using Eqs. (9) and (10).
- (2) Perform a global search over source locations to obtain a starting point for the nonlinear (Marquardt) algorithm.
- (3) Iterate until convergence of the cost function $\tilde{H}(\underline{\xi}, \underline{\eta}, B, \underline{\alpha})$:
 - (a) obtain an update for the positions in $\underline{\xi}$ in the Marquardt algorithm (the first time, the starting point from the global search is taken)
 - (b) iterate until convergence of $\tilde{H}(\underline{\xi}, \underline{\eta}, B, \underline{\alpha})$ for fixed $\underline{\xi}$:
 - (i) update B using Eq. (29),
 - (ii) iterate until convergence of $\tilde{H}(\underline{\xi}, \underline{\eta}, B, \underline{\alpha})$ for fixed $\underline{\xi}$ and B :
 - (A) update $\underline{\alpha}$ using Eqs. (16), (32), and (33),
 - (B) update $\underline{\eta}$ using Eqs. (15), (30), and (31).

In the global search in step (2), a regular grid with locations is computed. For each location, step (3b) is executed and the converging value of the cost function H for that location is computed. The location with the minimum value of the cost function is taken as starting point in step (3). In step (2), alternative initialization procedures can be used, as outlined in [Uutela et al. \(1998\)](#).

Results

The coupled dipole model was applied in two simulation studies and to one experimental data set. In the first simulation study, a symmetric dipole pair was simulated representing three different functional areas: the somatosensory cortex, the auditory cortex, and the visual cortex. In the second simulation study, data from two dipoles in the visual cortex of the same hemisphere were generated in different ratios of activity. The experimental data consisted of visual evoked field (VEF) MEG data. The visual stimulus in this experiment consisted of a checkerboard pattern, presented either in one hemifield or full-field to the subject.

Table 1
Locations of simulated sources in simulation 1

	Position source left (cm)			Orientation source left		
	x	y	z	x	y	z
Somatosensory	1.63	3.80	3.18	-0.83	0.47	-0.29
Visual	-6.37	1.80	-2.82	-0.44	0.22	0.87
Auditive	0.63	4.30	-0.82	0.00	0.00	1.00

The positions of the sources are relative to the center of the spherical volume conductor. Positions and orientations of the sources were taken symmetric, i.e. with opposite y coordinates. The direction of the x axis is forward, the y axis to the left, and the z axis upwards.

Simulation study 1

In the first simulation study, activity from two single dipole sources was generated. Three surrogate data sets were produced: in the first data, the left source was simulated, in the second, the right source and the third data set contained simulated data from both sources. The locations of the sources were taken symmetric and varied over the visual, auditory, and somatosensory cortices. True locations of these cortices were based on experimentally located positions (see Table 1). Two basic source time functions were used to generate the data, see Eqs. (36) and (37). For each location, 100 sweeps were generated. The sample rate used was 625 Hz, and a time window of 32 ms was analyzed. All data sets consisted of simulated dipole activity and additional white noise with varying signal to noise ratio, SNR equal to 1/3, 1, 3, and 9. The SNR is defined as the ratio between the matrix powers of the surrogate signal and the surrogate white noise:

$$SNR = \frac{\text{tr}(R_{\text{sur}}^t R_{\text{sur}})}{\text{tr}(E_{\text{sur}}^t E_{\text{sur}})} \quad (34)$$

The first data set contained activity from the left source with STF1, the second activity from the right source with STF1, and the third data set contained activity from both sources, both having STF2.

The matrix $\mathbf{A}(\eta, \xi)$ contained the forward fields of both dipoles, and \mathbf{B} contained the two normalized basic STFs. The coupling matrices for the three data sets were

$$C_1 = \begin{pmatrix} \alpha_1 & 0 \\ 0 & 0 \end{pmatrix}, C_2 = \begin{pmatrix} 0 & 0 \\ \alpha_2 & 0 \end{pmatrix}, C_3 = \begin{pmatrix} 0 & \alpha_3 \\ 0 & \alpha_4 \end{pmatrix} \quad (35)$$

Both input STFs were 10 Hz sinusoids:

$$STF_1(t) = \frac{1}{n_1} \sin(20\pi t) \quad (36)$$

$$STF_2(t) = \frac{1}{n_2} \left(\sin\left(20\pi t - \frac{\pi}{4}\right) + 0.35 \right) \quad (37)$$

where n_1 and n_2 are the normalization constants, $n_1 = \sqrt{11.5003}$ and $n_2 = \sqrt{10.1852}$. The following coupling parameter values were used

$$\alpha_1 = 1000n_1 \quad (38)$$

$$\alpha_2 = 1000n_1 \quad (39)$$

$$\alpha_3 = 1000n_2 \quad (40)$$

$$\alpha_4 = 1000n_2 \quad (41)$$

The absolute values of the magnitudes do not influence the performance of the different localization methods. Only the relative amount of noise, indicated by the SNR, counts. Therefore, the α values were chosen such that the absolute magnitudes were comfortable in the analysis. In Fig. 2, the input STFs are plotted as function of time. Four different source localization analyses were performed: the three data sets in three separate analyses as presented in De Munck et al. (2002) and all data sets simultaneously in the CDM. In the separate analyses, the

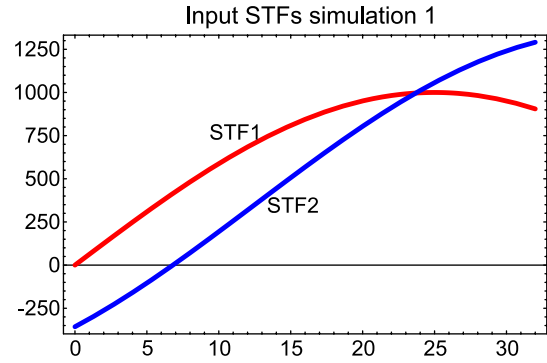


Fig. 2. The two basic input STFs for simulation 1 multiplied by 1000, which is the amplitude in all data sets.

estimation of the source parameters was performed based on the simulated number of sources: one source was localized in data sets 1 and 2, and two sources were estimated in data set 3. The grid for the global search consisted of 100 locations, resulting in 100 possible starting points for data sets 1 and 2 and $100 \times 99/2 = 4950$ possible starting combinations for data set 3. In the CDM analysis, two sources, two STFs, and nonzero elements of the coupling matrices in Eq. (35) were estimated. The same grid was used for the global search, yielding $100 \times 99 = 9900$ possible starting combinations of the two sources, because the order of the sources is important in the CDM. Average errors in position and orientation of the estimated dipoles as well as in magnitude of the estimated source time functions were computed for all four analyses. The averages were taken over the sweeps and over both sources (position and orientation) or both STFs (magnitude).

For all three cortex locations, the errors show a similar pattern: the integrated analysis yields a lower error than the separate analyses. Depending the distance between the sources, this difference in performance varies. The errors in position, orientation, and magnitude show a similar pattern; therefore, only the position error is shown in Fig. 3. In Fig. 3a, the average position error for the simulated dipoles in the somatosensory cortex is shown; in Fig. 3b, the auditory cortex; and in Fig. 3c, the visual cortex. Clearly, the difference in performance between the separate approach and the CDM is largest for two active dipoles in the visual cortex (Fig. 3c). The reason for this is that the (lateral) distance between the simulated visual dipoles is smallest. Therefore, localizing the two sources in the classical way will be hampered by the reasons mentioned in the introduction. For all analyses, Fig. 3 shows an improvement (slightly) in position error for the integrated model, indicating that adding more data into the parameter estimation is advantageous.

Simulation study 2

In the second simulation study, two sources in the visual cortex, one in the striate and one in the extrastriate cortex, were simulated in five different ratios of activity. Positions and orientations were taken from experimentally located sources, resulting in the sources being 3 cm apart from each other (Table 2). As in simulation 1, data consisted of simulated dipole activity and white noise with varying SNR, $SNR = 1/3, 1, 3,$ and 9. Each data set contained 100 sweeps, the sample frequency was 625 Hz, and a time window of 32 ms was analyzed. The input source time functions were two sinusoids,

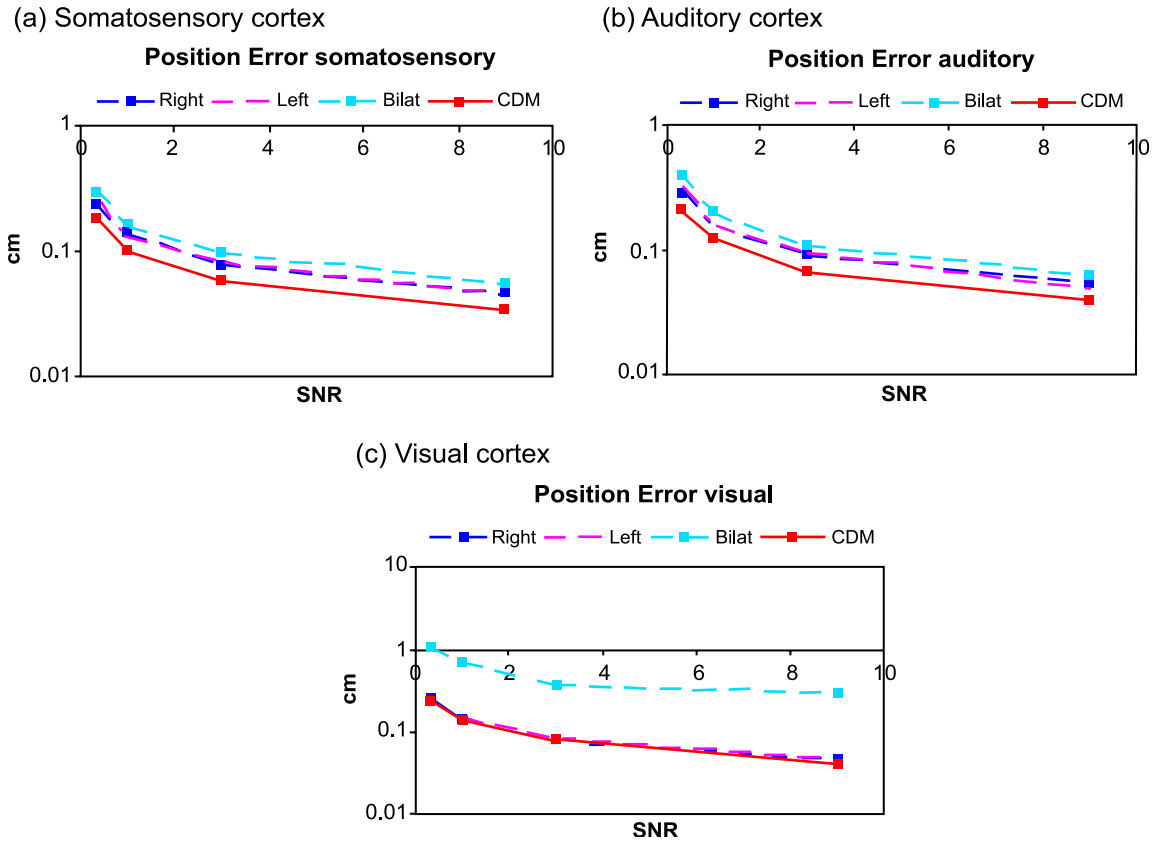


Fig. 3. Average position errors in simulation 1. The errors are given in cm on a logarithmic scale. The dashed lines correspond to the separate analyses and the solid line indicates results of the CDM. Right corresponds to the data set with only the right source active, left to the data set with the left dipole active, and BiLat to the data set with both sources active. (a) Position errors of the localized sources in the somatosensory cortex. (b) Position errors of the localized sources in the auditory cortex. (c) Position errors of the localized sources in the visual cortex.

15 Hz for the striate source and 20 Hz for the extrastriate source

$$STF_1(t) = \frac{1}{n_3} \sin(30\pi t) \tag{42}$$

$$STF_2(t) = \frac{1}{n_4} \sin(40\pi t). \tag{43}$$

where $n_3 = \sqrt{10.4013}$ and $n_4 = \sqrt{8.49828}$ are the normalization constants. The five data sets were generated using the coupling matrices

$$C_1 = \begin{pmatrix} 1000n_3 & 0 \\ 0 & 0 \end{pmatrix}, C_2 = \begin{pmatrix} 750n_3 & 0 \\ 0 & 250n_4 \end{pmatrix}, \tag{44}$$

$$C_3 = \begin{pmatrix} 500n_3 & 0 \\ 0 & 500n_4 \end{pmatrix}, C_4 = \begin{pmatrix} 250n_3 & 0 \\ 0 & 750n_4 \end{pmatrix},$$

$$C_5 = \begin{pmatrix} 0 & 0 \\ 0 & 1000n_4 \end{pmatrix},$$

Fig. 4 shows the two input STFs. Six source localization analyses were performed: the five data sets separately (De Munck et al., 2002) and all five data sets in the integrated model.

Furthermore, in the CDM analysis, diagonal coupling matrices with two unknowns were used for all data sets. In other words, in the CDM analysis, no advantage was taken of the knowledge that data

sets 1 and 5 contain activity of only one dipole, while this information was exploited in the separate analyses.

For the global search, the same grid as in the first simulation study was used. This resulted in 100 possible starting locations for the separate analyses of data sets 1 and 5, 4950 possible combinations for data sets 2, 3, and 4, and 9900 possible combinations for the CDM (as the order of the sources is of importance in the simultaneous model).

Outliers in the estimated sources were discarded. The outlier criteria used are

$$\text{position error} > 7 \text{ cm} \tag{45}$$

$$\text{distance between sources} < 0.5 \text{ cm} \tag{46}$$

$$\text{magnitude error (relative power)} > 10 \tag{47}$$

The first criterium designates localized sources in implausible positions, which would be discarded in experimental analysis. The

Table 2
Locations of simulated sources in simulation 2

	Position (cm)			Orientation		
	x	y	z	x	y	z
Striate	-6.37	1.30	-1.82	-0.15	0.59	0.79
Extrastriate	-5.37	3.30	-3.82	0.70	0.60	-0.40

The positions of the sources are relative to the center of the spherical volume conductor. The direction of the x axis is forward, the y axis to the left, and the z axis upwards.

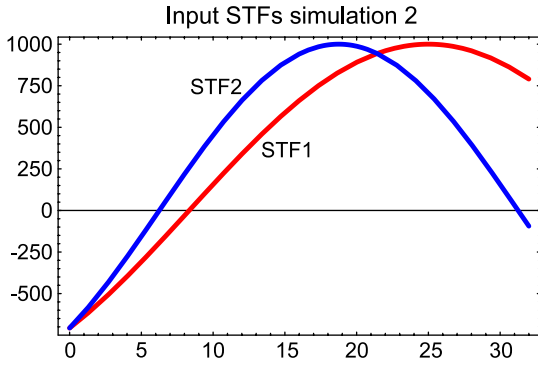


Fig. 4. The two basic input STFs for simulation 2 multiplied by 1000, the maximum amplitude (data sets 1 and 5).

latter two criteria often concur and indicate two coinciding sources, usually having opposite orientations and unreasonably high magnitudes, as discussed in Introduction. In Table 3, the numbers of outliers in the different localizations are given: only the three data sets containing two active sources yielded outliers in the separate analyses. The simultaneous CDM did not yield any outliers.

Average position errors, orientation errors, and magnitude errors were computed for all six analyses. The averages were computed over the 100 sweeps (minus the outlying sweeps) and over both sources and both STFs.

As in the first simulation, the graphs of the three types of error resemble each other. Fig. 5 demonstrates the position errors for all analyses. The errors in the separate analyses can be divided into two groups; data set 1 and 5, which contain only one active source, show a lower error than the remaining three data sets. This reflects the common feature that one source is easier localized than two sources. Nevertheless, the CDM yields the lowest position error. Compared to the separate analyses, using the CDM, the position error drops approximately by a factor of 10 for data sets 2, 3, and 4. For data sets 1 and 5, there is still an improvement of roughly a factor of 1.5 in the position error.

Experimental data

The CDM was applied to experimental MEG data of a visual evoked field experiment. The visual stimuli consisted of checkerboard pattern onsets, presented either in the left or the right hemifield or full-field, thus yielding three data sets per subject. The separate analyses of this kind of conditions show nearby localized sources with similar orientations for the different conditions, indicating that the assumption of common sources is plausible. Moreover, the estimated orientations are opposite (Di Russo et al., 2002; Kenemans

Table 3
The number of outliers in the six source localizations in simulation 2

SNR	1/3	1	3	9
Data set 1	0	0	0	0
Data set 2	6	1	1	1
Data set 3	0	2	1	4
Data set 4	16	16	19	18
Data set 5	0	0	0	0
CDM	0	0	0	0

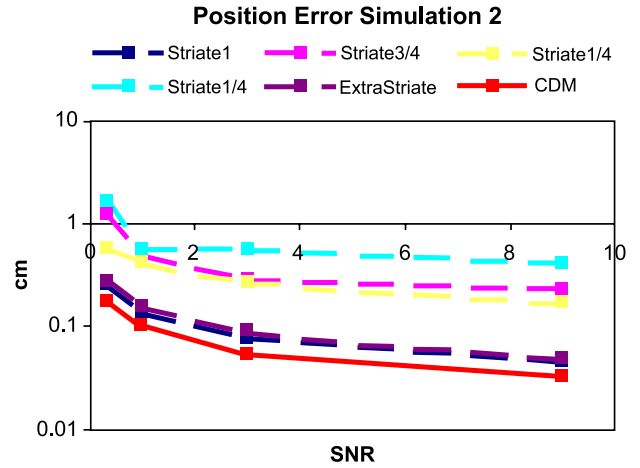


Fig. 5. The average position error of the localized sources in the simulation 2. Striate1 corresponds to data set 1, Striate3/4 to data set 2, Striate1/2 to data set 3, Striate1/4 to data set 4, and ExtraStriate to data set 5. The errors are given in centimeters on a logarithmic scale. The dashed lines correspond to the separate analyses and the solid line indicates results of the CDM.

et al., 2000); therefore, the solutions to the separate IPs are susceptible for the canceling dipole problem. For this reason, the behavior of the separate analyses and the CDM is compared using these visual data.

Data of five subjects were considered in this study. The time window of analysis was set to 80–112 ms post stimulus. The sample rate was 625 Hz, the number of trials was 400 in each data set. Similar to simulation 1, the three data sets were analyzed separately, yielding three sets of estimated parameters, and the CDM was applied to all three data sets simultaneously, yielding one solution with estimated common spatial and common temporal parameters.

The check size was 6'. Checks of this size mainly activate the striate cortex in the chosen time interval (Di Russo et al., 2002; Ossenblok et al., 1994). As expected, hemifield stimuli first activate the contralateral hemisphere, with a peak at around 90–95 ms. However, between 10 and 15 ms (Saron and Davidson, 1989) or 20 ms later (Steger et al., 2001), the ipsilateral hemisphere is activated as well by inter-hemispheric transfer. In sum, to describe the hemifield data, two sources are needed, having in the CDM two different STFs: a contralateral STF and an ipsilateral STF. The contralateral STF was also used to describe the time courses of both sources in the bilateral data set, because these stimuli will activate both hemispheres directly (Kenemans et al., 2000), although maybe even faster (Steger et al., 2001). This yielded the following basic and coupling matrices:

$$A = (DF_{left} \quad DF_{right}), B = \begin{pmatrix} STF_{contra} \\ STF_{ipsi} \end{pmatrix} \quad (48)$$

$$C_{lh} = \begin{pmatrix} 0 & \alpha_2 \\ \alpha_1 & 0 \end{pmatrix}, C_{rh} = \begin{pmatrix} \alpha_3 & 0 \\ 0 & \alpha_4 \end{pmatrix}, C_{ff} = \begin{pmatrix} \alpha_5 & 0 \\ \alpha_6 & 0 \end{pmatrix}, \quad (49)$$

where “lh” corresponds to the left hemifield stimulation, “rh” to the right hemifield stimulation, and “ff” to the full-field stimulation.

Table 4
Estimated locations for subject 5 in the experimental study

	Position source left (cm)			Orientation source left			Orientation source right		
	x	y	z	x	y	z	x	y	z
Data set LH 23	-5.21	1.29	0.94	0.26	0.96	0.11	0.26	-0.96	0.11
Data set LH 102	-5.21	1.29	0.94	0.26	0.96	0.11	0.26	-0.96	0.11
Data set RH 23	-6.14	1.21	0.17	0.17	0.76	0.62	0.00	0.12	0.99
Data set RH 102	-5.72	0.32	0.11	0.06	0.88	0.47	0.05	-0.96	-0.27
Data set FF 23	-4.42	0.00	-1.15	0.25	-0.05	-0.97	-0.25	0.05	0.97
Data set FF 102	-5.14	1.43	0.89	0.31	-0.77	0.56	0.28	-0.96	0.08
CDM	-5.25	1.44	0.85	0.30	0.72	0.62	0.28	-0.95	0.12

The positions of the localized sources are relative to the center of the spherical volume conductor. The positions of the two sources are symmetric. The direction of the x axis is forward, the y axis to the left, and the z axis upwards.

In all the analyses, a semisymmetric source pair was fitted. Semisymmetric sources have symmetric locations (as in Di Russo et al., 2002; Kenemans et al., 2000), but their orientations are free. Nevertheless, the estimated orientations are nearly symmetric (Table 4).

The number of locations in the regular grid for the global search for the starting location of the semisymmetric dipole source was varied over 23, 102, and 466 points in one hemisphere, corresponding to mesh sizes of 4.2, 2.6, 1.5 cm, respectively.

The solutions to the separate IPs changed when the number was increased from 23 to 102 grid points, but remained the same for the increase from 102 to 466 points. The simultaneous model, though, yielded the same solutions for all three grids. This shows

that the CDM is less sensitive to local minima in the cost function.

The results of the separate analyses varied considerably over subjects. For subjects 1 and 2, the separate analyses yielded plausible solutions for all three conditions for both 23 and 102 grid points.

For subject 3, all three separate solutions to the IP consisted of a pair of canceling, coinciding sources (intermediate distance < 0.01 cm). Even using a global search with 466 grid points yielded these implausible solutions for all three separate models. Subject 4 yielded for the right hemifield data set a physiologically plausible solution for all grids. For the coarse grid, the sources in the full-field data set were localized in the cerebellum. For 102 grid

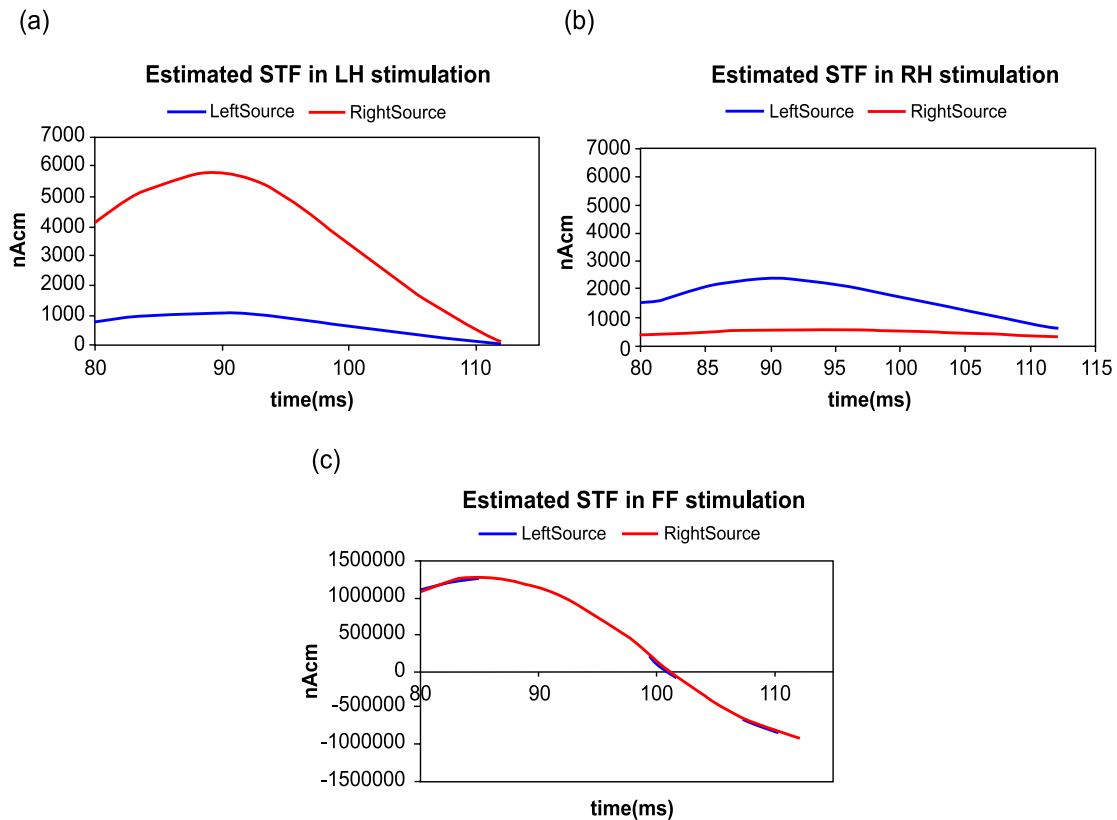


Fig. 6. Estimated STFs of the semisymmetric sources resulting from the separate analyses using a global search with 23 grid points in the experimental study (subject 5). The time indicated is the post stimulus time in milliseconds. The unit on the vertical axis is nAcm. (a) The estimated STFs for the left hemifield stimulation data set. (b) The estimated STFs for the right hemifield stimulation data set. (c) The estimated STFs for the full-field stimulation data set.

points, this problem was resolved and the solutions were localized in the visual cortex. The locations of the sources in the left hemifield data set showed a plausible location, though the ipsilateral orientation differs from the usual lateral direction for all grids. The corresponding amplitude is very small; therefore, the total influence of this orientation on the cost function is very small.

Subject 5 (see Table 4) yielded a solution consisting of a canceling dipole pair for the full-field data set when the coarse grid was used. For the denser grids, this data set yielded an interpretable solution. The right hemifield data set yielded a location in the visual cortex for 23 grid points, though the ipsilateral orientation was unusual. For 102 and 466 grid points, these sources were localized nearer to the midsagittal plane (1.2 cm in between). For all grids, left hemifield data set yielded plausible solutions.

The simultaneous model yielded for all five subjects plausible solutions for all conditions for all grids.

Summarizing, for the coarse grid, 5 of the 15 separate analyses resulted in an implausible solution, and for the denser grids, 3 of the 15 conditions yielded a non-interpretable solution, whereas the simultaneous model only yielded plausible solutions.

The results of subject 5 are representative for the type of errors that can occur in the separate solutions; therefore, the analyses of this subject for the coarse (23 points) and the dense (102 points) grid and the CDM solution are presented. The estimated locations and orientations of the sources for the seven different localizations are reported in Table 4. The estimated STFs are shown in Figs. 6–8. Fig.

6 shows the STFs estimated in the separate analyses using the coarse grid, Fig. 7 the estimated STFs for the dense grid, and Fig. 8 displays the estimated STFs for the simultaneous model that did not change with the number of grid points.

In Fig. 6c, an example of the canceling dipole problem is shown: the magnitudes are unrealistically high, the corresponding locations in Table 4 coincide, and the estimated orientations are opposite. For the coarse grid, the RH data set does not yield the usual lateral orientation for the ipsilateral source. This orientation does not have a substantial influence on the cost function, because the corresponding amplitude (Fig. 6b) is rather small. The amplitudes in the different analyses for the RH data set vary. In Fig. 7b (dense grid), the estimated amplitudes are larger than the amplitudes shown in Figs. 6b (coarse grid) and 8b (CDM). The corresponding distance to the midsagittal plane for the dense grid (0.32 cm) is smaller than for the coarse grid and the CDM (1.21 and 1.44 cm, respectively). This may indicate a slight cancellation of dipole activity: the sources are closer and the amplitudes are higher for the dense grid.

Discussion

The coupled dipole model provides a method to solve the inverse problem by analyzing multiple MEG data sets simultaneously when these data sets contain common sources or common source time functions. This way, more data are used and more constraints (assumptions) are made to solve and stabilize the IP.

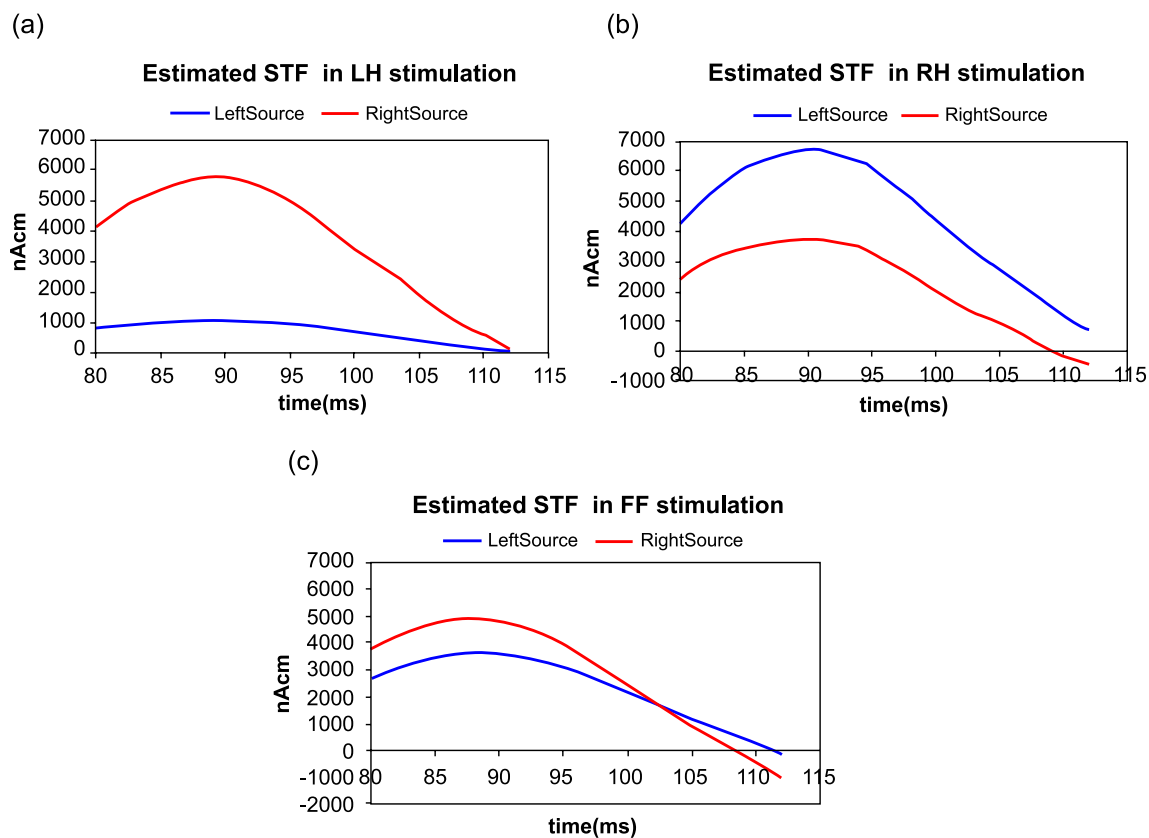


Fig. 7. Estimated STFs of the semisymmetric sources resulting from the separate analyses using a global search with 102 grid points in the experimental study (subject 5). The time indicated is the post stimulus time in milliseconds. The unit on the vertical axis is nAcm. (a) The estimated STFs for the left hemifield stimulation data set. (b) The estimated STFs for the right hemifield stimulation data set. (c) The estimated STFs for the full-field stimulation data set.

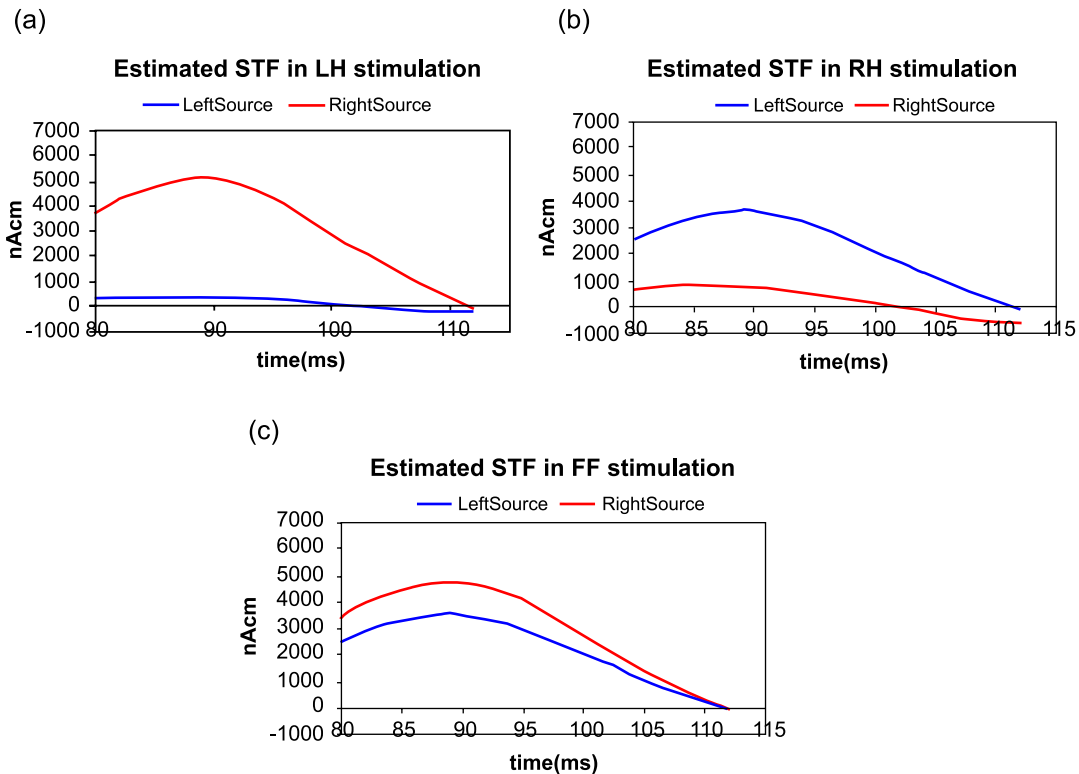


Fig. 8. Estimated STFs of the semisymmetric sources resulting from CDM analysis in the experimental study (subject 5). The time indicated is the post stimulus time in milliseconds. The unit on the vertical axis is nAcm. (a) The estimated STFs for the left hemifield stimulation data set. (b) The estimated STFs for the right hemifield stimulation data set. (c) The estimated STFs for the full-field stimulation data set.

The results of the first simulation show that the position error decreases when the integrated model is used instead of the separate models. The gain in accuracy depends on the locations (intermediate distance) of the sources to be localized and was largest for the simulated sources in the visual cortex.

Simulation 2 displays a considerable improvement in source localization for the CDM, studying two active dipoles in the visual cortex in five different ratios of activity. For one of the five data sets considered, a quarter striate and three quarters extrastriate activity, the position error drops by a factor of 10 when the CDM is used instead of a single model. Moreover, outliers only occurred in the separate analyses of data sets 2, 3, and 4, while the CDM did not yield any outliers (see Table 3). In Fig. 5, it can be seen that the position error of data set 4 is higher for SNR = 3 than it is for SNR = 1. A similar feature was found in the orientation and magnitude error. This contradicts the fact that for higher SNR the error decreases. The reason for this slight increase in error lies in the outlier problem. For all SNR values in data set 4, some sweeps were marked as outlier (45) and discarded. However, some other sweeps, not indicated as outlier, also showed a rather large position error (>2 cm), but within the outlier criterium of 7 cm. For SNR = 1, the number of these semi-outlying sweeps was lower than for SNR = 1/3 and SNR = 3. Because these sweeps raise the average error remarkably, this difference between SNR = 1 and the other SNR values explains the error shape in Fig. 5. Increasing the number of sweeps considerably or redefining the outlier criteria should eliminate this problem. This shows that the choice of outlier criteria is delicate. Nonetheless, this outlier problem is not present in the CDM (Table 3), which is an important advantage of the integrated approach regarding the stability of the solution.

The application of the CDM to experimental VEF data showed that in 5 (coarse grid) or 3 (dense grid) of the 15 conditions considered, no interpretable solution was obtained without using the CDM. The classic (separate) analysis of all but one of these conditions yielded a canceling dipole source pair, and one condition yielded a localized visual source pair in the cerebellum (coarse grid). The CDM yielded invariably plausible solutions. This demonstrates that the CDM is not sensitive for minima in the cost function that correspond to a canceling dipole pair. The underlying reason may be that these minima of the separate cost functions occur at different locations for different conditions and will therefore not produce a minimum in the simultaneous cost function.

Another advantage of the simultaneous model is the direct comparability of the estimated magnitudes. Because all parameters are estimated in one analysis, the magnitudes between conditions can directly be compared (Fig. 8), while the separate analyses (Figs. 6 and 7) use for different conditions different scalings and it is difficult to compare the absolute magnitudes between conditions. This difference in scaling is caused by the depth bias (the mutual dependence of depth and amplitude) and possible slight cancellation of the sources (cf. RH for the coarse grid) and the differences in STF shapes between conditions.

Summarizing, the experimental application showed that simultaneously estimating the amplitudes and locations in the three data sets yields more stable and comparable estimated parameters, while separate models are more vulnerable for implausible minima and yield in general estimated magnitudes and positions that vary over data sets.

The estimation procedure for the signal parameters presented in this paper is computationally intensive due to the nested iterations in

the estimation procedure. It is our intention to improve the method to overcome this drawback.

Designing the coupling matrices is subject to the choice (or a priori knowledge) of the user. Different users may want to design the coupling matrices in a different way. This is both a flexibility property of the model and a subjectivity of the CDM. The user can make more or less assumptions by adapting the dimension of the coupling matrices, as was shown in the example in Eqs. (2) and (3). Such assumptions, in fact, are also made when similar data sets are analyzed using separate analyses: results are compared afterwards and conclusions are drawn about the similarity of sources and source time functions in the different data sets. The CDM now provides a way to put this knowledge a priori in the source localization method, which relatively increases the SNR. If the user is not sure about certain similarities, the coupling matrices should be extended to less assumptions. In the second simulation study, the robustness of the CDM was tested by applying less assumptions than possible (fitting two sources when only one was active in data sets 1 and 5), and it was shown that the CDM still estimates the sources and STFs well.

A possible extension of the CDM would be the simultaneous analysis of data sets of different subjects and/or different conditions. If it is assumed that the spatial and temporal covariances differ only slightly over subjects and conditions (Bijma et al., 2003; De Munck et al., 2002), and can therefore be fixated, this extension is rather straightforward. This kind of extension will be helpful if one is interested in grand averages of, for example, amplitude functions or source positions as in cognitive neuroscience (Di Russo et al., 2002; Kenemans et al., 2000).

In all, the CDM combines multiple data sets and extra constraints into one integrated model to solve and stabilize the ill-posed inverse problem in MEG/EEG, yielding interpretable solutions, in cases where separate models not always yield plausible solutions.

Appendix A. Dimensions and variables

The dimensions are defined as

$$I—\# \text{ sensors} \quad (50)$$

$$J—\# \text{ time samples} \quad (51)$$

$$K_q—\# \text{ trials in data set } q \quad (52)$$

$$K—\# \text{ trials in all data sets} \quad (53)$$

$$P—\# \text{ basic sources} \quad (54)$$

$$Q—\# \text{ data sets} \quad (55)$$

$$Y—\# \text{ amplitude parameters} \quad (56)$$

$$Z—\# \text{ basic STFs} \quad (57)$$

and the variables as

$$\underline{\alpha}—Y \times 1 \text{ vector containing amplitude parameters} \quad (58)$$

$$\underline{\eta}—3P \times 1 \text{ vector with sources orientations} \quad (59)$$

$$\underline{\xi}—3P \times 1 \text{ vector with source locations} \quad (60)$$

$$A(\underline{\xi}, \underline{\eta})—I \times P \text{ forward field matrix of basic dipoles} \quad (61)$$

$$\mathbf{A}—IQ \times IP \text{ matrix : } \mathbf{I}_Q \otimes A \quad (62)$$

$$B—Z \times J \text{ basic STF matrix, with basic STFs as rows} \quad (63)$$

$$\mathbf{B}—Z \times J \text{ prewhitened STF matrix} \quad (64)$$

$$C_q—P \times Z \text{ coupling matrix for data set } q \quad (65)$$

$$\mathbf{C}—PQ \times Z \text{ stacked coupling matrices} \quad (66)$$

$$E_q^k—I \times J \text{ noise matrix of trial } k \text{ in data set } q \quad (67)$$

$$\mathbf{I}_n—n \times n \text{ identity matrix} \quad (68)$$

$$R_q^k—I \times J \text{ data matrix of trial } k \text{ in data set } q \quad (69)$$

$$R_q—I \times J \text{ model matrix for data set } q \quad (70)$$

$$\bar{R}_q—I \times J \text{ average data matrix for data set } q \quad (71)$$

Appendix B. ML estimators for X and T

This derivation uses the following two matrix derivatives (Magnus and Neudecker, 1995, chapter 9)

$$d_X(|X|) = |X| \text{tr}(X^{-1} dX)$$

and

$$d_X(X^{-1}) = -X^{-1} dX X^{-1}.$$

The derivative of $L(X, T, \underline{\xi}, \underline{\eta}, \underline{\alpha}, B)$ in Eq. (7) with respect to X is

$$\begin{aligned} d_X L &= L \times \left[\frac{-\frac{JK}{2} d|X|}{|X|} + d_X \left(-\frac{1}{2} \text{tr} \left[\sum_{q=1}^Q \sum_{k=1}^{K_q} (R_q^k - \bar{R}_q B)^t X^{-1} \right. \right. \right. \\ &\quad \left. \left. \left. \times (R_q^k - \bar{R}_q) T^{-1} \right) \right] \right) \\ &= \frac{1}{2} L \times \left[\frac{-JK|X| \text{tr}(X^{-1} dX)}{|X|} \right. \\ &\quad \left. + \text{tr} \left[\sum_{q=1}^Q \sum_{k=1}^{K_q} (R_q^k - \bar{R}_q)^t X^{-1} dX X^{-1} (R_q^k - \bar{R}_q) T^{-1} \right] \right] \\ &= \frac{1}{2} L \times \left[\text{tr} \left(\left[-JK + \sum_{q=1}^Q \sum_{k=1}^{K_q} X^{-1} (R_q^k - \bar{R}_q) T^{-1} \right. \right. \right. \\ &\quad \left. \left. \left. \times (R_q^k - \bar{R}_q)^t \right] X^{-1} dX \right) \right] \quad (72) \end{aligned}$$

The optimal spatial covariance matrix, \hat{X}_{ML} , is obtained when $d_X L = 0$, that is, when

$$\begin{aligned} & \left[-JK + \sum_{q=1}^Q \sum_{k=1}^{K_q} \hat{X}_{ML}^{-1} (R_q^k - \bar{R}_q) T^{-1} (R_q^k - \bar{R}_q)^t \right] \hat{X}_{ML}^{-1} \\ & = 0 \Leftrightarrow \hat{X}_{ML} = \frac{1}{JK} \sum_{q=1}^Q \sum_{k=1}^{K_q} (R_q^k - \bar{R}_q) T^{-1} (R_q^k - \bar{R}_q)^t, \end{aligned} \quad (73)$$

provided that \hat{X}_{ML} is nonsingular. Similarly for T , the estimator becomes

$$\hat{T}_{ML} = \frac{1}{IK} \sum_{q=1}^Q \sum_{k=1}^{K_q} (R_q^k - \bar{R}_q)^t X^{-1} (R_q^k - \bar{R}_q). \quad (74)$$

Appendix C. ML estimator for B

Although the rows in B are normalized, the ML estimator for B is derived as if B were unconstrained. The rows are normalized afterwards.

$$\begin{aligned} d_B L &= \frac{1}{2} L \times \text{tr} \left[\sum_{q=1}^Q \sum_{k=1}^{K_q} (AC_q dB)^t X^{-1} (R_q^k - AC_q B) T^{-1} \right. \\ & \quad \left. + (R_q^k - AC_q B)^t X^{-1} AC_q dB T^{-1} \right] \\ &= L \times \text{tr} \left[\sum_{q=1}^Q \sum_{k=1}^{K_q} T^{-1} (R_q^k - AC_q B)^t X^{-1} AC_q dB \right]. \end{aligned} \quad (75)$$

Setting this derivative to zero yields the estimator for B :

$$\begin{aligned} & \sum_{q=1}^Q \sum_{k=1}^{K_q} T^{-1} (R_q^k - AC_q \hat{B}_{ML})^t X^{-1} AC_q = 0 \\ & \Leftrightarrow \sum_{q=1}^Q \sum_{k=1}^{K_q} (R_q^k)^t X^{-1} AC_q \\ &= \sum_{q=1}^Q \sum_{k=1}^{K_q} (AC_q \hat{B}_{ML})^t X^{-1} AC_q \\ & \Leftrightarrow \hat{B}_{ML} = \left(\sum_{q=1}^Q K_q C_q^t A^t X^{-1} AC_q \right)^{-1} \sum_{q=1}^Q \sum_{k=1}^{K_q} C_q^t A^t X^{-1} (R_q^k)^t, \end{aligned} \quad (76)$$

provided that $\sum_{q=1}^Q K_q C_q^t A^t X^{-1} AC_q$ is invertible. After this estimator has been calculated, the STFs in B are normalized.

Appendix D. ML estimator for orientation parameters η in A

The source parameters in A can be split into the linear orientation parameters $\underline{\eta}$, and the nonlinear position parameters $\underline{\xi}$. If all P sources are modeled as single dipoles or symmetric source pairs, $\underline{\eta}$ and $\underline{\xi}$ will both be $3P \times 1$ vectors. If P semisymmetric source pairs (symmetric location, free orientation) are used, $\underline{\eta}$ will be $6P \times 1$ and $\underline{\xi}$ will be $3P \times 1$. For notational

clarity, $\underline{\eta}$ and $\underline{\xi}$ will both be assumed to be $3P \times 1$. For the case of semisymmetric sources, the dimensions have to be adjusted correspondingly. The linear parameters $\underline{\eta}$ are estimated in the usual ML sense; setting the derivative of L equal to zero. The nonlinear parameters $\underline{\xi}$ are determined using the Marquardt algorithm. The derivative of L with respect to $\underline{\eta}$ is calculated by first computing $d_A L$ and subsequently applying the chain rule.

$$\begin{aligned} d_A L &= \frac{1}{2} L \times \text{tr} \left[\sum_{q=1}^Q \sum_{k=1}^{K_q} (dAC_q B)^t X^{-1} (R_q^k - AC_q B) T^{-1} \right. \\ & \quad \left. + (R_q^k - AC_q B)^t X^{-1} dAC_q B T^{-1} \right] \\ &= L \times \text{tr} \left[\sum_{q=1}^Q \sum_{k=1}^{K_q} C_q B T^{-1} (R_q^k - AC_q B)^t X^{-1} dA \right]. \end{aligned} \quad (77)$$

Writing $\eta = (\eta_1, \dots, \eta_{3P})$ and applying the chain rule for the source parameter η_p yields

$$d_{\eta_p} L = L \times \text{tr} \left[\sum_{q=1}^Q \sum_{k=1}^{K_q} C_q B T^{-1} (R_q^k - AC_q B)^t X^{-1} \frac{\partial A}{\partial \eta_p} \right] d\eta_p \quad (78)$$

To obtain the ML estimate for η_p , this derivative is set to zero.

$$\begin{aligned} d_{\eta_p} L = 0 & \Leftrightarrow \text{tr} \left[\sum_{q=1}^Q \sum_{k=1}^{K_q} C_q B T^{-1} (R_q^k - AC_q B)^t X^{-1} \frac{\partial A}{\partial \eta_p} \right] = 0 \\ & \Leftrightarrow \text{tr} \left[\sum_{q=1}^Q \sum_{k=1}^{K_q} C_q B^{-1} (R_q^k)^t X^{-1} \frac{\partial A}{\partial \eta_p} \right] \\ &= \text{tr} \left[\sum_{q=1}^Q \sum_{k=1}^{K_q} C_q B T^{-1} B^t C_q^t A^t X^{-1} \frac{\partial A}{\partial \eta_p} \right] \end{aligned} \quad (79)$$

Because the basic field matrix A is linear in $\underline{\eta}$, it can be written as

$$A = \sum_{p=1}^{3P} \frac{\partial A}{\partial \eta_p} \eta_p \quad (80)$$

where $\partial A / \partial \eta_p$ is independent of $\underline{\eta}$. Eq. (79) holds for $p = 1, \dots, 3P$ and substituting Eq. (80) into Eq. (79) yields

$$\begin{aligned} & \text{tr} \left[\sum_{q=1}^Q \sum_{k=1}^{K_q} C_q B T^{-1} (R_q^k)^t X^{-1} \frac{\partial A}{\partial \eta_p} \right] \\ &= \text{tr} \left[\sum_{q=1}^Q \sum_{p'=1}^{3P} K_q C_q B T^{-1} B^t C_q^t \frac{\partial A^t}{\partial \eta_{p'}} X^{-1} \frac{\partial A}{\partial \eta_p} \right] \eta_{p'} \text{ for all } p \\ & \Leftrightarrow \Phi \underline{\eta} = \phi \end{aligned} \quad (81)$$

where

$$\Phi_{p_1, p_2} = \text{tr} \left[\sum_{q=1}^Q K_q C_q B T^{-1} B^t C_q^t \frac{\partial A^t}{\partial \eta_{p_2}} X^{-1} \frac{\partial A}{\partial \eta_{p_1}} \right] \quad (82)$$

and

$$\phi_p = \text{tr} \left[\sum_{q=1}^Q \sum_{k=1}^{K_q} C_q B T^{-1} (R_q^k)^t X^{-1} \frac{\partial A}{\partial \eta_p} \right]. \quad (83)$$

The linear parameters η_p are solved from the linear system in Eq. (81).

Appendix E. ML estimator for amplitude parameters in C

Analogous to the moment parameters, the amplitude parameters $\underline{\alpha}$ in the coupling matrices C_q are estimated using the chain rule. Writing $\underline{\alpha} = (\alpha_1, \dots, \alpha_Y)$ the derivative with respect to α_y is

$$\begin{aligned} d_{\alpha_y} L &= \frac{1}{2} L \times \text{tr} \left[\sum_{q=1}^Q \sum_{k=1}^{K_q} (A d_{\alpha_y} C_q B)^t X^{-1} (R_q^k - A C_q B) T^{-1} \right. \\ &\quad \left. + (R_q^k - A C_q B)^t X^{-1} A d_{\alpha_y} C_q B T^{-1} \right] \\ &= L \times \text{tr} \left[\sum_{q=1}^Q \sum_{k=1}^{K_q} B T^{-1} (R_q^k - A C_q B)^t X^{-1} A d_{\alpha_y} C_q \right] \\ &= L \times \text{tr} \left[\sum_{q=1}^Q \sum_{k=1}^{K_q} B T^{-1} (R_q^k - A C_q B)^t X^{-1} A \frac{\partial C_q}{\partial \alpha_y} \right] d\alpha_y. \end{aligned} \quad (84)$$

The ML estimators for α_y satisfy

$$\begin{aligned} d_{\alpha_y} L = 0 &\Leftrightarrow \text{tr} \left[\sum_{q=1}^Q \sum_{k=1}^{K_q} B T^{-1} (R_q^k - A C_q B)^t X^{-1} A \frac{\partial C_q}{\partial \alpha_y} \right] = 0 \\ &\Leftrightarrow \text{tr} \left[\sum_{q=1}^Q \sum_{k=1}^{K_q} B T^{-1} (R_q^k)^t X^{-1} A \frac{\partial C_q}{\partial \alpha_y} \right] \\ &= \text{tr} \left[\sum_{q=1}^Q \sum_{k=1}^{K_q} B T^{-1} B^t C_q^t A^t X^{-1} A \frac{\partial C_q}{\partial \alpha_y} \right]. \end{aligned} \quad (85)$$

Similar to the decomposition of A in Eq. (80), we can decompose C_q due to the linearity in $\underline{\alpha}$:

$$C_q = \sum_{y=1}^Y \frac{\partial C_q}{\partial \alpha_y} \alpha_y \quad (86)$$

for $q = 1, \dots, Q$, with $\partial C_q / \partial \alpha_y$ independent of $\underline{\alpha}$. Eq. (85) holds for $y = 1, \dots, Y$. Formula (86) is substituted in formula (85), and we obtain

$$\begin{aligned} &\text{tr} \left[\sum_{q=1}^Q \sum_{k=1}^{K_q} B T^{-1} (R_q^k)^t X^{-1} A \frac{\partial C_q}{\partial \alpha_y} \right] \\ &= \text{tr} \left[\sum_{q=1}^Q \sum_{y'=1}^Y K_q B T^{-1} B^t \frac{\partial C_q^t}{\partial \alpha_{y'}} A^t X^{-1} A \frac{\partial C_q}{\partial \alpha_y} \right] \alpha_{y'} \text{ for all } y \\ &\Leftrightarrow \Psi \alpha = \psi, \end{aligned} \quad (87)$$

where

$$\Psi_{y_1 y_2} = \text{tr} \left[\sum_{q=1}^Q K_q B T^{-1} B^t \frac{\partial C_q^t}{\partial \alpha_{y_2}} A^t X^{-1} A \frac{\partial C_q}{\partial \alpha_{y_1}} \right] \quad (88)$$

and

$$\psi_y = \text{tr} \left[\sum_{q=1}^Q \sum_{k=1}^{K_q} B T^{-1} (R_q^k)^t X^{-1} A \frac{\partial C_q}{\partial \alpha_y} \right]. \quad (89)$$

This linear system solves the amplitude parameters $\underline{\alpha}$ in C_q .

References

- Achim, A., Bouchard, S., 1997. Toward a dynamic topographic components model. *Electroencephalogr. Clin. Neurophysiol.* 103, 381–385.
- Bijma, F., de Munck, J.C., Huizenga, H.M., Heethaar, R.M., 2003. A mathematical approach to the temporal stationarity of background noise in MEG/EEG measurements. *NeuroImage* 20 (1), 233–243.
- de Munck, J.C., Vijn, P.C.M., Lopes da Silva, F.H., 1992. A random dipole model for spontaneous brain activity. *IEEE Trans. Biomed. Eng.* 39 (8), 791–804.
- de Munck, J.C., Huizenga, H.M., Waldorp, L.J., Heethaar, R.M., 2002. Estimating stationary dipoles from MEG/EEG data contaminated with spatially and temporally correlated background noise. *IEEE Trans. Signal Process.* 50 (7), 1565–1572.
- de Munck, J.C., Bijma, F., Gaura, P., Sieluzycy, C., Branco, M.I., Heethaar, R.M., in press. A mathematical description of habituation effects in multichannel MEG/EEG data. *IEEE Trans. Biomed. Eng.*
- Di Russo, F., Martinez, A., Sereno, M.I., Pitzalis, S., Hillyard, S.A., 2002. Cortical sources of the early components of the visual evoked potential. *Hum. Brain Mapp.* 15 (2), 95–111.
- Field, A.S., Graupe, D., 1991. Topographic component (parallel factor) analysis of multichannel evoked potentials: practical issues in trilinear spatiotemporal decomposition. *Brain Topogr.* 3, 407–423.
- Huizenga, H.M., de Munck, J.C., Waldorp, L.J., Grasman, R.P.P.P., 2002. Spatiotemporal EEG/MEG source analysis based on a parametric noise covariance model. *IEEE Trans. Biomed. Eng.* 49 (6), 533–539.
- Kenemans, J.L., Baas, J.M.P., Mangun, G.R., Lijffijt, M., Verbaten, M.N., 2000. On the processing of spatial frequencies as revealed by evoked potential source modeling. *Clin. Neuroph.* 111 (6), 1113–1123.
- Magnus, J.R., Neudecker, H., 1995. *Matrix Differential Calculus with Applications in Statistics and Econometrics*, Revised Edition. John Wiley and Sons, Chichester.
- McGille, C.D., Aunon, J.I., 1987. *Analysis of event-related potentials*. In: Gevins, A.S., Remond, A. (Eds.), *Methods of Analysis of Brain Electrical and Magnetic Signals*, EEG Handbook. Elsevier, Amsterdam, pp. 131–169.
- Möcks, J., 1988. Topographic components models for event related potentials and some biophysical considerations. *IEEE Biomed. Eng.* 35 (6), 482–484.
- Ossenblok, P., Reits, D., Speckreijse, H., 1994. Check size dependency of the sources of the hemifield-onset evoked-potential. *Ophthalmologica* 88 (1), 77–88.

- Saron, C.D., Davidson, R.J., 1989. Visual evoked potential measures of interhemispheric transfer time in humans. *Behav. Neurosci.* 103 (5), 1115–1138.
- Scherg, M., Von Cramon, D., 1985. Two bilateral sources of the late AEP as identified by a spatio-temporal dipole model. *Electroencephalogr. Clin. Neurophysiol.* 62, 32–44.
- Steger, J., Imhof, K., Denoth, J., Pascual-Marqui, R.D., Steinhausen, H.C., Brandeis, D., 2001. Brain mapping of bilateral visual interactions in children. *Psychophysiology* 38 (2), 243–253.
- Turetsky, B., Raz, J., Fein, G., 1990. Representation of multi-channel evoked potential data using a dipole component model of intracranial generators: application to the auditory P300. *Electroencephalogr. Clin. Neurophysiol.* 76, 540–556.
- Uutela, K., Hämäläinen, M., Salmelin, R., 1998. Global Optimization in the Localization of Neuromagnetic Sources. *IEEE Biomed. Eng.* 45 (6), 716–723.
- Wang, K.M., Begleiter, H., Porjesz, B., 2000. Trilinear modeling of event-related potentials. *Brain Topogr.* 12 (4), 263–271.